# Proppant embedment in coal and shale: Impacts of stress hardening and sorption

Sheng Zhi*, Derek Elsworth

*Department of Energy and Mineral Engineering, EMS Energy Institute and G3 Center, Pennsylvania State University, University Park, PA 16802, USA*

A B S T R A C T

During methane production in CBM reservoirs, the influence of proppant embedment and permeability damage cannot be neglected – especially where the wall-rock is soft. Effective stresses are elevated during methane recovery, increasing both normal loading stress and confinement and simultaneously overprinting sorption-induced volumetric strains. Experiments and analytic modeling are conducted to define key mechanisms controlling these competitive effects. We independently measure overall sample compaction (external LVDT) and local strain (strain gauge) in the matrix to deconvolve proppant embedment in a propped fracture for different conditions of confining stress. The results show symptomatic behaviors of elastic (shale) and elastoplastic (coal) responses of embedment. Different from shale, the evolution of embedment is convex upwards with increased stress where indented depth increases more rapidly as loading stress increases under constant confinement. In addition, a stress-hardening effect is found to play a pivotal role in determining the characteristics of indentation, which are examined in terms of evolution profiles, deformation regimes, embedment slopes, curvatures, yield points and irreversible indentations. Based on the experimental observations a semianalytical model predicts indentation and the evolution of propped permeability under recreated in-situ stress conditions. A simplified case study is conducted to further illustrate the evolution of aperture and permeability of a propped fracture in CBM reservoirs. The modeling results suggest that proppant embedment is significantly overestimated if the variable stress-hardening (VSH) effect is neglected, especially when effective stress is large. Moreover, a decrease in indentation depth possibly occurs during late stage methane production, resulting in a reversal/recovery in fracture closure. This is because desorption-induced shrinkage becomes the predominant effect, causing an increase in aperture and a reduction in the indented volume of proppant. The resulting recovery in permeability implies that the propped coal fracture has the potential to optimally facilitate methane production as a pathway, even at high closure stresses generated by methane drainage.

## 1. Introduction

Hydraulic fracturing involving the injection of proppants into the resulting fracture is a critical technology in the production of unconventional reservoirs and has been implemented in 67% of methane production wells within the USA (Bandara et al., 2019). Unconventional energy sources, including shale gas, coalbed methane and methane hydrates, have the potential to be the largest contributors to the continued growth of hydrocarbon outputs by 2040 (Wanniarachchi et al., 2017). The essence of hydraulic fracturing is to generate propped fractures by the injection of highly pressurized fluid containing a slurry of proppants into a tight reservoir – enhancing the resulting fracture permeability. However, proppant embedment, which may occur in deep (high stress) and soft rock formations, may result in more than a 100-fold conductivity reduction, leading to severe decline in methane production (Penny et al., 2012). It is well known that hydraulic fracturing is the key to large-scale commercial exploitation of CBM – despite the presumed impacts of proppant embedment. Unlike for shale gas, only limited studies have explored the impacts of proppant embedment on the performance of CBM reservoirs (Geng et al., 2015). This work addresses this knowledge gap.

Extensive observations and analyses have investigated the factors that influence proppant embedment. Measurements on fractures in sandstone have demonstrated the influence of closure stress, proppant material, size, concentration and hydraulic fracturing fluids (Lacy et al., 1998; Penny, 1987). The results suggest that indentation into soft and wet sandstone could reduce fracture aperture by half when the loading stress is greater than 48 MPa (7000 psi). Proppants with a heterogeneous distribution embed deeper than those with a uniform placement, while the conductivity for a heterogeneous proppant distribution is higher at relatively low closure stresses due to the larger fracture porosity (Hou et al., 2017). Morphological analyses of surface roughness evaluate the impact of surface asperities on proppant embedment. Results indicate that surface roughness has little impact on propped permeability when the concentration of proppant packing is high within the fracture (Stoddard et al., 2011; Volk et al., 1981). Shearing tests on rough propped fractures result in deeper embedment than for smooth fractures due to the impact of dilation (Tang and Ranjith, 2018). In addition, proppant indentation depth increases almost linearly with increasing shearing displacement. The propped permeability of fractures in coal is influenced by the elastic modulus of the coal and proppant size (Li et al., 2018) and the nature of the gas as sorbing or

non-sorbing (Kumar et al., 2015a). Various experimental observations are matched by analytical models. These include embedment represented as elastic deformation via Hertzian elastic contact models (Chen et al., 2017; Guo et al., 2017; Y. Li et al., 2018; Mueller et al., 2015; Zhang and Hou, 2016) and also considering elastoplastic or fully plastic deformation induced by surface indentation in relatively soft material or under considerable mechanical compression (Kogut and Etsion, 2002; Li and Gu, 2009; Song and Komvopoulos, 2013; Zhao et al., 2000).

Although many factors that influence embedment or propped permeability have been investigated, the effects of in-situ stress conditions have, to date, been neglected. Extraction of methane from laterally confined reservoirs yields both elevated effective stresses normal to the fracture surface and an increase in confinement. Simultaneously, sorption-induced volumetric strains develop as fluid pressure drops, changing the fracture aperture (Kumar et al., 2015a; Wu et al., 2018). We explore the complex outcome of these effects on proppant embedment that are not previously reported. In this study, we make precise measurements of proppant embedment into coal under varying stress conditions. Both experimental and analytical results are presented to define the evolution of proppant embedment during gas simulated production.

## 2. Experimental methodology

We complete experiments to precisely measure indention depths of proppant into coal/shale surfaces on nine specimens under different confining and loading conditions. Sample preparation and experimental techniques are introduced in the following.

### 2.1. Sample preparation

Cylindrical coal samples with a diameter of 25.4 mm (1 in.) were cored from block samples collected at a depth of ~200 m from a coal mine in southwest Illinois. Coring was at low speed to avoid damage to the horizontal beddings with each specimen then cut by circular saw to a standard length (25.4–38.1 mm (1–1.5 in.)). The top and bottom surfaces of the trimmed samples were ground smooth and parallel for testing, using a face grinder.

Proximate analysis identified the samples as high volatility bituminous coal. The weight percentages of moisture, fixed carbon and volatile matter were 3%, 41% and 37%, respectively. The calorific values of 25,073–26,158 kJ/kg were measured on #200 mesh powdered particles. The average density of the coal under unconfined conditions was 1238 kg/m$^3$ (Table 1).

### 2.2. Experimental setup

Fig. 1 shows how the samples and proppants are deployed for the measurement of proppant embedment. Two individual syringe pumps were used to independently control confining stress and axial stress, up to 35 MPa (resolution to ± 0.1 kPa). Either distilled water or hydraulic oil were used as hydraulic fluids and a high-strength PVC rubber jacket separated the samples from the fluids. Axial displacement of the piston was measured externally using a linear variable displacement transducer (LVDT) in contact with the moving piston (resolution of 1 μm).

**Table 1**
Proximate analysis for Illinois coal.

| Moisture | Fixed carbon | Volatile matter | Ash |
|---|---|---|---|
| 3% | 48% | 42% | 7% |
| Calorific value | 25,073–26,158 kJ/kg | | |
| Rank | High volatility bituminous | | |
| Density | 1238 kg/m$^3$ | | |

Axial loading was applied at only 5 kPa/s to avoid any unexpected physical damage induced by rapid compression.

Two of the trimmed coal samples were used together in any single experiment (Fig. 1). A resistance strain gauge was bonded to the geometrical center of lateral surface of a coal sample to measure the matrix deformation. A monolayer of 20/40 mesh proppants were sandwiched between the two samples to represent a proppant-supported fracture. These were then restrained by low-friction tape and two steel platens that delivered the loading stress. The assembly was then lubricated by oil on the lateral surface and sheathed in a high-strength polyvinyl chloride (PVC) rubber jacket. The term "specimen" will be used to refer to this assembly of coal samples sandwiching proppant in the following. The loading stress, piston displacement and coal matrix compaction were then monitored and recorded simultaneously, at a sampling rate of 10 Hz. Proppant embedment was eventually obtained from the difference between overall compaction of the composite specimen (LVDT) and the shortening of the matrix samples (strain gauge).

### 2.3. Standard test procedure

The experiments are categorized into two sets: represented by either single or cyclic loading. The goal of the single load testing was to investigate the influence of axial loading stress on proppant embedment under different confining conditions. The experimental configuration for five coal specimens and a control group (shale) are summarized in Table 2. If conducted without confining stress, the axial loading stress was limited to 10 MPa to avoid crushing - considering the relatively low shear strength of coal. For the cases with confining stresses of 3, 6 and 9 MPa, the applied maximum closure stress was increased to 20 MPa. The cyclic loading explored cumulative damage and its effect in exaggerating proppant embedment. This simulates a multi-staged production/injection schedule (e.g. MECBM and $CO_2$-ECBM production). The loading pattern was designed to incorporate five repeated loading-and-unloading cycles, in which the loading and unloading rates were retained as ± 5 kPa/s – identical to that in the single loading tests. Three confining stresses of 0, 3, 9 MPa were selected in the cyclic loading scenarios.

In the single loading test, the axial stress was capped at the target stress then slowly relieved. In the cyclic loading tests, the load was held at the designated maximum for five minutes to stabilize with creep effects before slowly decreasing to 2 MPa - with this process repeated a total of five times.

## 3. Experimental results

The evolution of proppant embedment is explored under different stress conditions. These characteristics include embedment profiles in different regimes, gradients of closure in these regimes, curvatures, yield points and irreversible indentation. The influences of loading stress, stress-hardening effects and cyclic loading are carefully analyzed.

### 3.1. Convex embedment profile

The external LVDT records the overall specimen compaction that consists of both proppant embedment and local strain of coal matrix. The latter is separately measured by the strain gauge. Thus, proppant embedment can be deconvolved from the difference between the total axial displacement and the compaction of the coal matrix. Fig. 2 shows a typical monitoring result. As loading stress increases to 10 MPa, the total axial displacement for T-001 reaches 0.54 mm, while the matrix compression is only 0.18 mm (0.31% strain). The resulting indentation into the coal (T-001 & T-002) and shale (T-003) are demonstrated in Fig. 3, showing how embedment accumulates as fracture closure stress increases. A remarkably deeper indentation is evident in coal than in shale. For coal specimens, the proppant indentation reaches
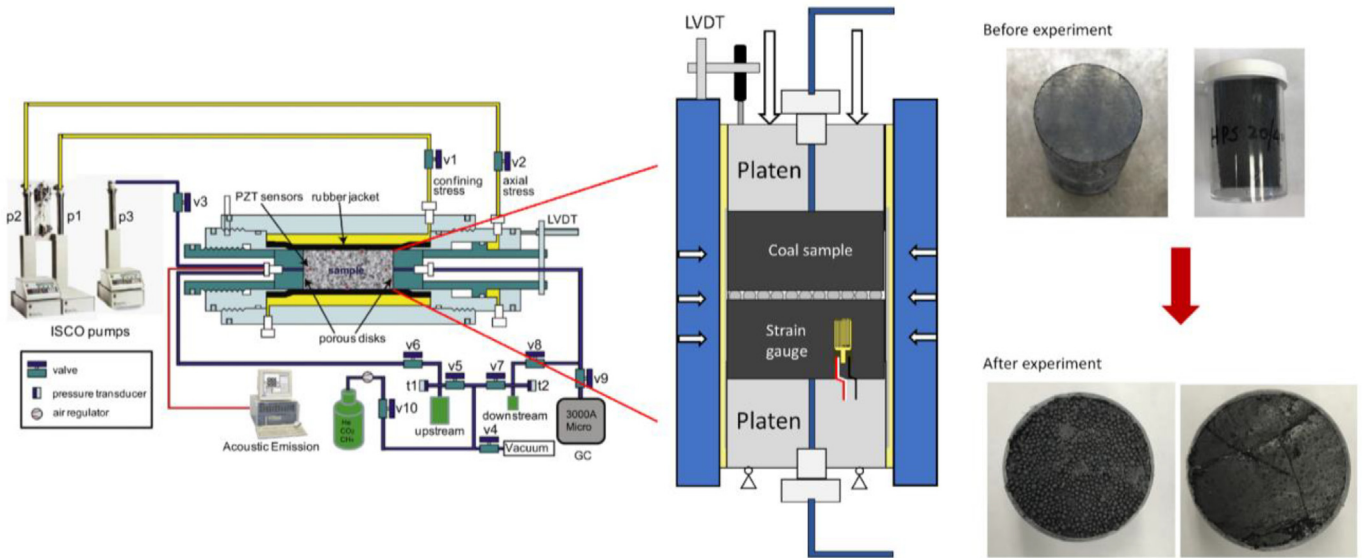
**Fig. 1.** Schematic of the experimental apparatus used in this study (partially adaption from Wang et al., 2011). Bottom right - propped fracture surfaces after loading.

**Table 2**
Summary of experimental configurations for the two suites of experiments.

| | Specimen# | Confining stress, MPa | Axial loading stress, MPa | Sample material | Loading cycles |
|---|---|---|---|---|---|
| Single loading tests | T-001 | 0 | 0–10 | Coal | 1 |
| | T-002 | 0 | 0–10 | Coal | 1 |
| | T-003 | 0 | 0–20 | Shale | 1 |
| | T-301 | 3 | 0–20 | Coal | 1 |
| | T-601 | 6 | 0–20 | Coal | 1 |
| | T-901 | 9 | 0–20 | Coal | 1 |
| Cyclic loading tests | T-001C | 0 | 2–10 | Coal | 5 |
| | T-301C | 3 | 2–10 | Coal | 5 |
| | T-901C | 9 | 2–10 | Coal | 5 |



**Fig. 3.** Proppant indentation in coal (T-001 & T-002) and shale (T-003). The results show clear differences in magnitude, pattern and the impact of yielding, in defining proppant evolution profiles.

0.163–0.173 mm as loading stress increases to 10 MPa. For shale, however, the indentation is merely 0.053 mm at 10 MPa. Even when the loading stress increases to 25 MPa, the indentation in shale reaches 0.118 mm that is still smaller than that in coal. Besides indentation depth, the profiles of the evolution of embedment are clearly different between coal and shale. The slope of the embedment increment in coal continues to increase during the loading process, while that for shale progressively decreases. It is the strength and elastic modulus that control the evolution of the pattern of embedment. The concave downwards curve for proppant embedment in hard materials is consistent with previous studies for sandstones (Lacy et al., 1998). However, the convex upwards profile for indentation in coal has not previously been reported.

In contact mechanics, there are multiple deformation regimes for a frictionless hard flat deformed by a rigid spherical indenter. The complete contact response consists of four deformation regimes - elastic, linear elastoplastic, nonlinear elastoplastic, and fully-plastic, as shown in Fig. 4. The indentation of a rigid spherical asperity into an elastic



**Fig. 2.** Typical monitoring results for overall compaction (external LVDT) and local strain (strain gauge) in coal. Note that the gap between the two curves represents the indentation of proppant into the two fracture surfaces.
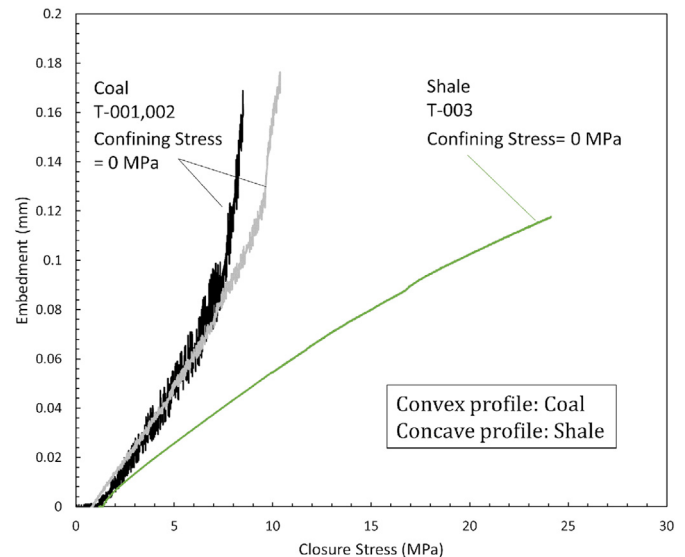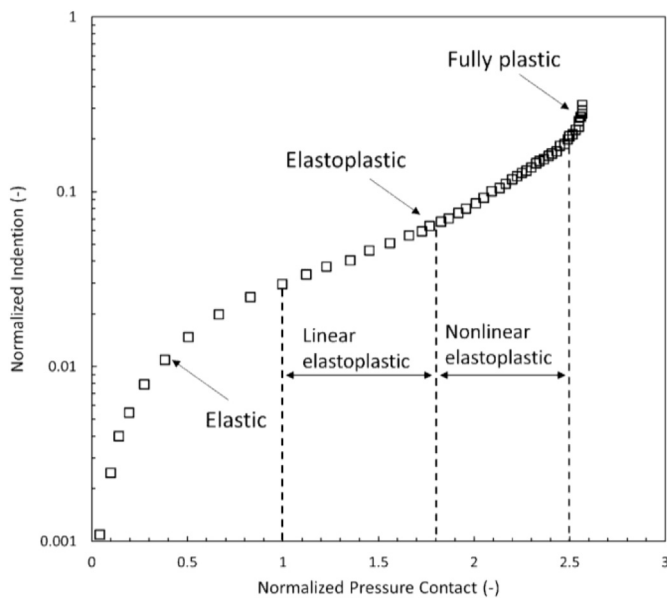
**Fig. 4.** Four regimes representing a complete contact response for a frictionless hard flat surface indented by a rigid spherical indenter (data adapted from Song and Komvopoulos, 2013).
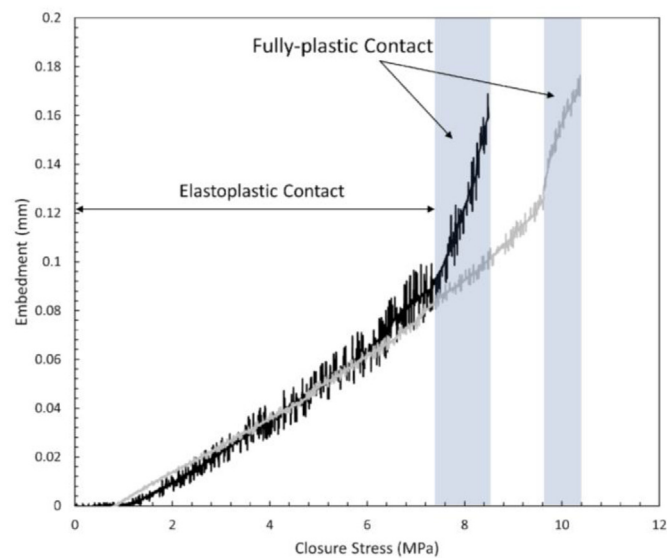


**Fig. 5.** Two main stages in the deformation of the coal surfaces due to indentation by proppant packs: elastoplastic and fully-plastic contacts.

half-space (Hertzian contact) shows a semi-logarithmic dependence on the loading stress. Hence, it is inferred that proppant embedment into shale occurs only within the elastic regimes. Conversely, the semilogarithmic profile is absent for the coal specimens. Instead of elastic deformation, the propped coal surfaces mostly sustain elastoplastic deformation, exhibiting a characteristic convex upwards profile of proppant embedment. Moreover, when the loading stress is increased to a threshold level, a rapid increase in embedment occurs, suggesting that a yield point has been transited. Fig. 5 shows these two main stages of deformation for the coal surfaces. For specimen T001, a relatively steadily increasing trend of proppant embedment is observed in the range 2–7.37 MPa. This is consistent with the form of the elastoplastic regime, yet the border between the linear and nonlinear elastoplastic regions is diffuse. Above 7.37 MPa, a rapid increase in indentation is observed, indicating that the form of the contact has transitioned into the fully-plastic regime. After the observation of plastic damage, axial

loading is suspended to avoid the complete crushing of the sample. The indented depth eventually reaches 0.17 mm, ~54% of the proppant radius. After the experiment, the rapid development of the plastic zone is only localized near the limited contact areas with the proppant, rather than throughout the entire coal matrix. Recall that Fig. 2 clearly shows a rapid increase in the LVDT deformation record and comparably, steady state matrix deformation following the yield stress. Similarly, For T002, the yield stress is 9.61 MPa and the elastoplastic regime ranges from 0 to 0.12 mm.

### 3.2. Stress-hardening effect

Although the prior results provide insight into the contrasting features of indentation in coal versus shale, the assumption of zero-confinement is unrealistic for underground engineering. The in-situ stress not only provides a closure stress normal to the fracture, but also restrains adjacent rocks via lateral confinement. Furthermore, this confinement varies with formation depth and fluid pressure. A large confining stress tends to increase rock capacity in accumulating elastic deformation at stress levels above unconfined yield strength, especially for soft rocks such as coal. This phenomenon can be described as a strain- or stress-hardening effect (Asef and Najibi, 2013; Morcote et al., 2010; Wang et al., 2013). We adopt the term "stress-hardening" in this work as the stress is always selected as the principal variable. Fig. 6 summarizes the evolution of embedment for T-001, 002, 301, 601 and 901 under different confinements. Under different confining stress, each specimen was tested with an increasing loading stress up to 25 MPa, unless fully plastic deformation was observed (via LVDT) below this stress. A description of the stress-hardening characteristics is provided in terms of embedment regime, embedment slope, elastic modulus and yield stresses, as shown in the following.

The unconfined specimens clearly exhibit both the elastoplastic and plastic indentation behaviors (see Section 3.1). For T-301, elastoplastic deformation persists until the loading stress reaches 17.67 MPa. After this yield point, a rapid increase in embedment is observed. For T-601, embedment increases rapidly after the yield point with an indistinct boundary between the elastoplastic and plastic regimes. A linear-elastoplastic zone predominates with a nonlinear elastoplastic zone appearing immediately before the inception of plastic damage. For T-901 (confining stress 9 MPa) a near-linear relationship between embedment and loading stress is observed. These results suggest that at a high confining stress (> 9 MPa here) elastoplastic indentation increases in an almost linear manner with loading stress, while at lower
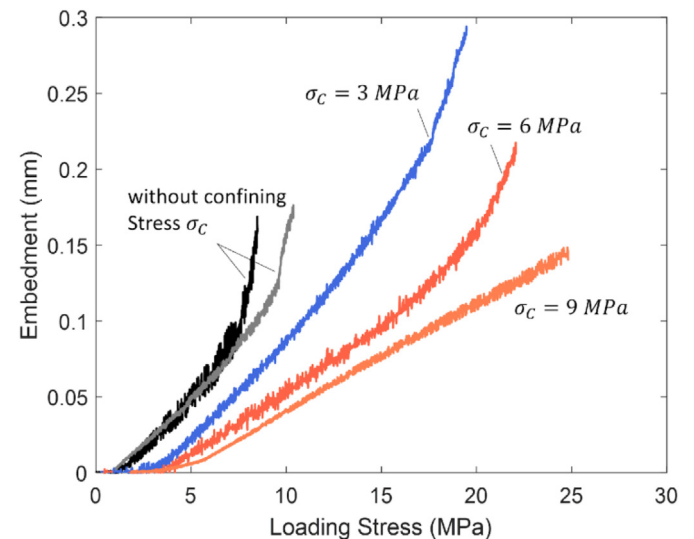


**Fig. 6.** Evolution of embedment for coal specimens under confinement of 0, 3, 6, 9 MPa.
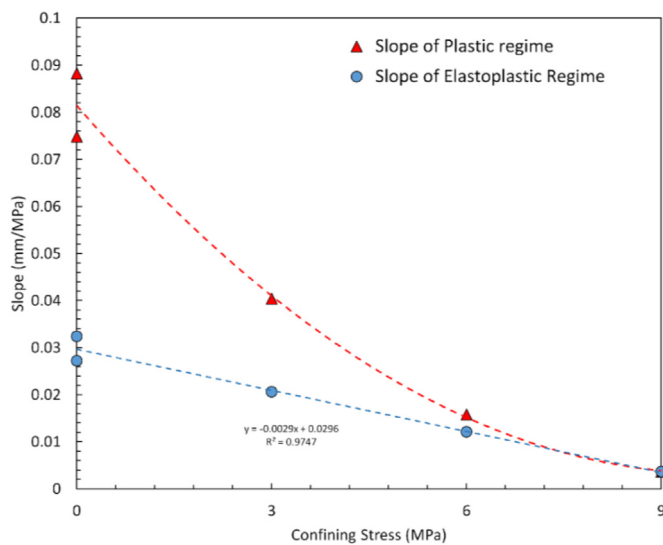
**Fig. 7.** Changes in slopes in both the elastoplastic and plastic regimes under different confining stresses. When confining stress increases, the slope of the embedment evolution curves significantly decreases. The results suggest that stress-hardening makes the coal stiffer and the fracture surfaces more impenetrable.

confinements the indentation has both elastoplastic (linear and non-linear) and plastic behaviors. This is presumably due to a strong stress-hardening effect that may extend the duration of elastic characteristics of the fracture surface. It is worth noting that high confinement does result in measurable friction between coal matrix and rubber jacket – maybe since lubricating oil and low-fraction Teflon tape have been used to control this.

The evolution of elastoplastic embedment is characterized by a convex upwards profile but with different slopes and curvatures. When confining stress increases, the slope of these embedment evolution curves significantly decreases, and the curvature gradually disappears. A quantitative analysis of the changes in slopes in both the elastoplastic and plastic regimes under different confining stresses is given in Fig. 7. The elastoplastic slopes present a near-linear relationship, showing a 7-fold decrease due to the increasing confinement from 0 to 9 MPa. The plastic slope exhibits a nearly quadratic relationship with confining stress. This strongly suggests that the stress-hardening effect increases

the stiffness of the coal and renders the fracture surfaces more impenetrable. Even after the initiation of fully-plastic damage, rapid indentation is partly alleviated by applying a high confining stress.

The elastic modulus of the coal samples is measured via the strain gauge attached on all coal samples. As a result of hardening, the elastic modulus of the coal samples displays a positive correlation with confining stress. Fig. 8(A) shows that the elastic modulus of the matrix increases from ~1.8 to 10.2 GPa when confining stress increases from 0 to 9 MPa. In addition, the fact that only linearly elastoplastic indentation can be observed at a confining stress of 9 MPa - the enhanced stiffness of the coal matrix is induced by the high confinement. These observations are congruent with the finding that shales with higher elastic moduli yield reduced indentation (Li et al., 2018). Fig. 8(B) shows how the coal strength is increased by confining stress. Yield points have been identified for confining stresses of 0, 3, 6 MPa, but no yielding occurs at a confining stress of 9 MPa. The yield stress increases from ~8.5 to 20.6 MPa when confining stress increases from 0 to 6 MPa.

### 3.3. Influence of cyclic loading

Fig. 9 shows changes in proppant embedment during cyclic loading at high confining stress (9 MPa). In the first cycle of loading, proppants embed a depth of 0.045 mm as the axial loading stress reaches 10 MPa. During the first unloading cycle, an obvious hysteresis is observed, with an irreversible indentation of 0.007 mm remaining. This shows that ~85% of the indentation is elastically recovered when the loading stress is relieved, with the remainder presumably being due to plastic deformation. The coexistence of both the elastic and plastic indentation regimes is reasonable since proppant embedment is in the elastoplastic regime during these loading/unloading processes. The successive four loading cycles are of consistent form but offset magnitude from the first cycle. The five unloading paths essentially overlap, causing no further evolution of irreversible indentation. The results suggest that the first cycle of loading and unloading determines the magnitudes of maximum indentation and irreversible indentation; the following loading-unloading cycles have little influence in exacerbating indentation at large confining stresses. Cyclic loading at a confining stress less than 3-MPa shows the similar result but with 23% irreversible indentation.

The aforementioned proppant embedment under confining stresses of 3 and 9 MPa shows elastoplastic behavior under repeated loading. To investigate the influence of plastic deformation on irreversible indentation, cyclic loading experiments were conducted under zero
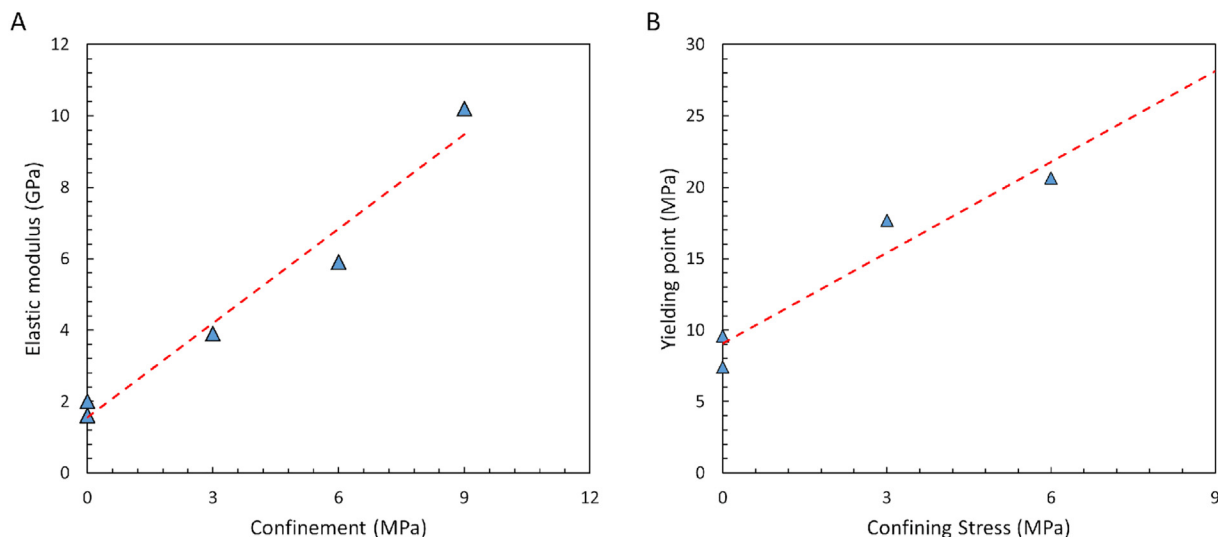


**Fig. 8.** (A) Elastic modulus of the tested coal samples increases with confining stress; (B) Yield stresses for confinements of 0, 3, 6 MPa, with no yielding occurring at a confinement of 9 MPa.
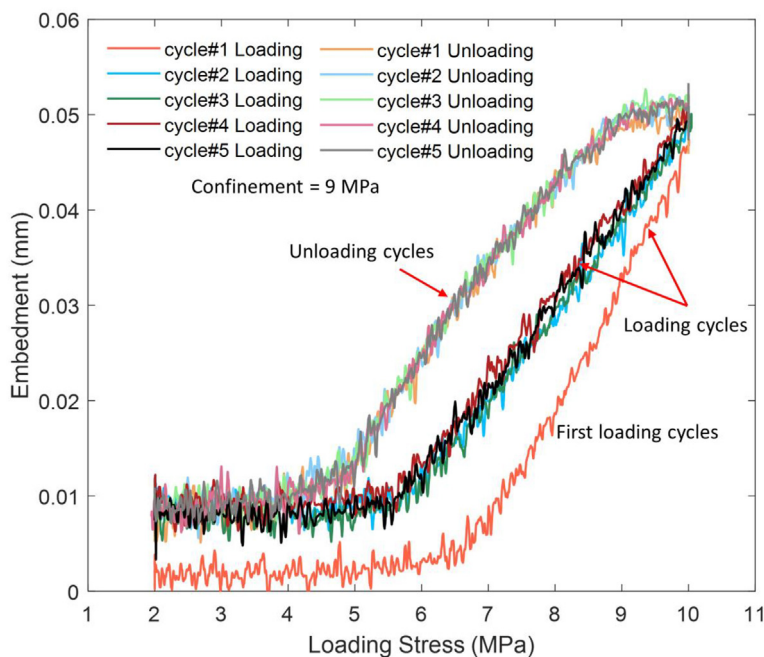
**Fig. 9.** Proppant embedment with cyclic loading at high confining stress (9 MPa). The first cycle of loading and unloading determines the maximum indentation and the magnitude of the irreversible indentation.
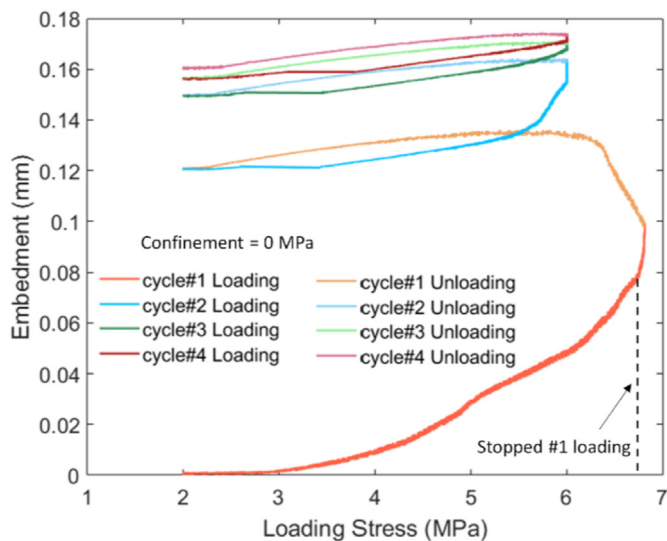


**Fig. 10.** Evolution of proppant embedment with cyclic loading (unconfined). In this case, cyclic loading exerts significant influence in deepening indentation and in reducing the stability of the coal matrix.

confinement for specimen T-001C, as shown in Fig. 10. Rapid plastic embedment occurs when the loading stress increases to 6.7 MPa. Plastic embedment continues to increase even after unloading, eventually reaching an irreversible indentation of ~0.12 mm. Following this, the maximum embedment increases with each successive loading cycle, with the hysteresis from each loading cycle now not overlapping. Sample T-001C completely ruptures during the fifth loading cycle. The results suggest that after the inception of plastic indentation, cyclic loading exerts a significant influence on the generation of deeper indentation and impacts the stability of the coal matrix. The changes in irreversible embedment for each successive cycle, for the three specimens, are summarized in Fig. 11.

## 4. Analytical modeling

Based on the experimental results, a semianalytical model is developed to predict both indentation and propped permeability under applied in situ stress conditions. A simplified case study is conducted to further illustrate the evolution of aperture and permeability of a propped fracture in a CBM reservoir.

### 4.1. Modeling of propped fracture

Representative models for coal with the evolution of elastoplastic contacts are summarized in Table 3. However, these are not able to capture the full range of characteristics evident in the observed elastoplastic embedment into coal surfaces. They represent either a simplified curve profile to that observed or require extra phenomenological fitting coefficients, especially when considering stress-hardening effect under in-situ stress conditions.

Mechanisms of elastoplastic deformation are complex, so derivation of an analytical solution remains infeasible. Instead, a semianalytical model is derived to represent the experimental observations reported previously and thus to further illuminate indentation mechanisms. Under realistic reservoir conditions, the extraction of methane yields both an increase in effective stresses normal to the fracture surface and an increase in confinement. The change in confining stress causes a varying stress-hardening (VSH) effect that is defined in this modeling. A template function uses a quadratic equation for data fitting of the proppant indentation under different confinements, shown as Fig. 12. The embedment evolution profiles are adjusted to eliminate the influence of friction. The plastic regime is also trimmed because this modeling focuses on elastoplastic deformation. Fig. 13 summarizes the results of linear regression for the complete set of testing conditions. Although the original template function has no constant coefficient, the constant coefficient $p_3$ is needed due to the noise in the experimental data. Coefficients $p_1$, $p_2$ and $p_3$ change with confinement, and are fitted by their corresponding second-order polynomial functions. Hence, the empirical quadratic function with varying coefficients $p_1$, $p_2$ and $p_3$ is obtained to describe the indentation depth as a function of both the loading stress and confinement.
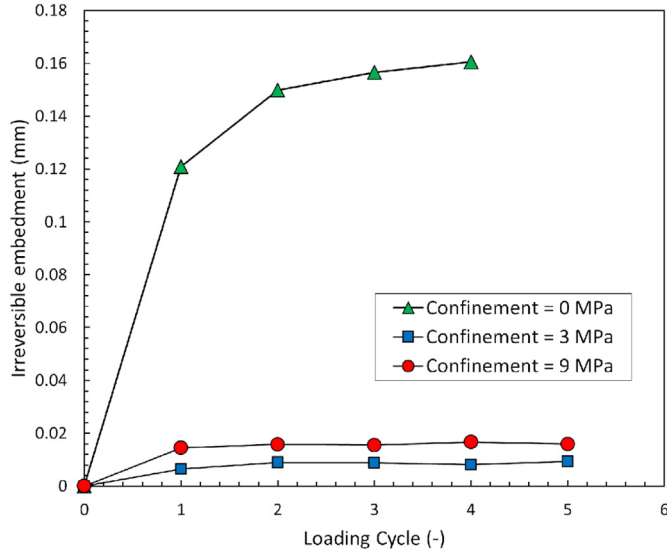
**Fig. 11.** Changes in irreversible embedment with loading cycles for three different confining stresses. Unconfined samples failed completely during the 5th loading cycle.

For a propped fracture with aperture $b_0 = 2R$ before closure, its initial fracture porosity $\varphi_0$ can be expressed as

$$\varphi_0 = \frac{b_0 A - \frac{4}{3}\pi R^3 \cdot \frac{A}{\pi R^2}\rho}{b_0 A} \tag{1}$$

where A is a unitary area of the fracture surface, $\rho$ is the proppant concentration as a %. Note that the proppant deformation is ignored due to the low elastic modulus of coal samples. When an indentation of depth $h$ occurs, the fracture porosity changes to

$$\varphi = \frac{(b_0 - 2h)A - \left(\frac{4}{3}\pi R^3 - V_i\right)\frac{A}{\pi R^2}\rho - 2hA}{b_0 A} \tag{2}$$

where $V_i = 2 \times \frac{1}{3}\pi h^2(3R - h)$ is the volume of the proppant embedded into the coal.

Subtracting Eq. (1) from Eq. (2) yields

$$\Delta\varphi = \frac{h^2}{3R^3}(3R - h)\rho - \frac{h}{R} \tag{3}$$

Based on the cubic law, the change in permeability of the proppant pack can be expressed as (Lee et al., 2010; Li et al., 2018)

$$\frac{k}{k_0} = \left(1 + \frac{\Delta\varphi}{\varphi_0}\right)^3 \tag{4}$$

where $k_0$ is the initial proppant permeability.

Considering that either $CH_4$ or $CO_2$ are sorptive gases, a sorption-induced strain $\varepsilon_s$ based on a Langmuir isothermal model can be written as

$$\varepsilon_s = \varepsilon_L \frac{p_f}{p_f + p_L} \tag{5}$$

where $p_f$ is the fluid pressure, $\varepsilon_L$ and $p_L$ are the Langmuir strain and Langmuir pressure constants, respectively.

Based on conservation of volume, a relationship between fluid pressure and proppant indentation $h_2$ can be expressed as

$$2A(h_1 - h_2) - \left\{\frac{2}{3}\pi h_1^2(3R - h_1) - \frac{2}{3}\pi h_2^2(3R - h_2)\right\}\frac{A}{4R^2}\rho = \frac{-\Delta\varepsilon_s}{\varphi_{f0}}2R\beta A \tag{6}$$

where the original indentation $h_1$ is a function of loading stress and confinement, $\Delta\varepsilon_s$ is the change in sorption-induced strain, $\varphi_{f0}$ is the initial porosity, and $\beta$ is an arbitrary shape factor. The new indentation depth $h_2$ can be recovered from this cubic equation. Eqs. (3) and (4) are then used to calculate the propped permeability with the calculated $h_2$.

### 4.2. Case study exploring propped permeability

During reservoir production, the effective loading stress normal to the fracture surface is elevated due to the decrease of fluid pressure, while the effective confining stress applied laterally on the surrounding coal is also increased. As a result, an increment in the effective loading stress prompts increased proppant embedment, but the increment in effective confining stress impedes proppant indentation - due to the stress-hardening effect. Simultaneously, the change in sorption-induced strain also influences the indented volume. When the coal matrix desorbs, the resulting shrinkage plays a critical role in decreasing the indented volume of the proppant. These competitive effects, illuminated in Fig. 14, are investigated in this case study. It is assumed that for a
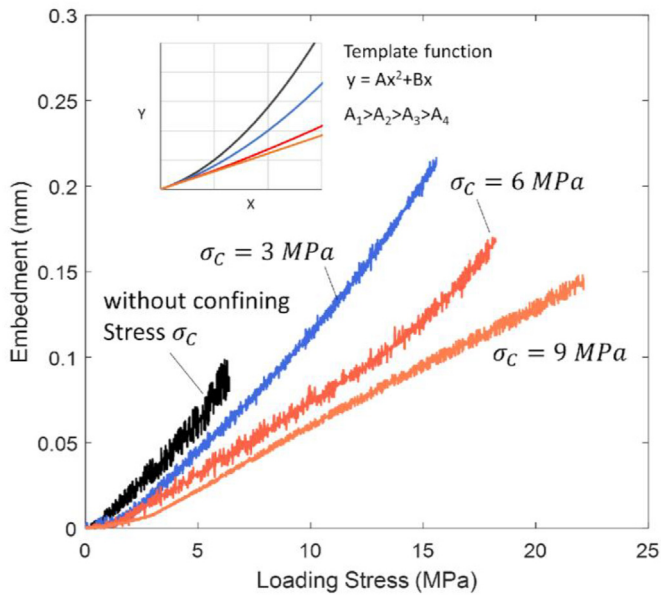
**Table 3**
Summary of models representing proppant embedment in fracture walls.

| | Governing equations | Remarks |
|---|---|---|
| Hertzian elastic model | $h = \left(\frac{3}{4}\frac{\sigma_a}{E^* R^{\frac{1}{2}}}\right)^{\frac{2}{3}}$ <br> where h is the proppant indentation depth, $\sigma_a$ is the mean contact stress on the fracture, $E^*$ is the Hertzian elastic modulus, and R is the proppant radius. | The linear elastic model based on contact mechanics. Similar works are in Guo et al., 2017 and Chen et al., 2017. |
| Kumar's model (Kumar et al., 2015b) | $h = R\left(1 - \sqrt{1 - \frac{\sigma'}{\pi C}}\right)$ <br> where $\sigma'$ is the effective stress and C is the cohesion of coal. | Assumed that the proppant is evenly distributed on the coal fracture surface. Modified model can be found in Zhi et al., 2018. |
| Li's model (Li et al., 2015) | $h = 1.04 D_1(K^2\sigma_a)^{\frac{2}{3}}\left[\left(\frac{1}{E^*}\right)^{\frac{2}{3}} - \left(\frac{1-\nu_1^2}{E_1}\right)^{\frac{2}{3}}\right] + D_2\frac{\sigma_a}{E_2}$ <br> where $D_1$ is the diameter of the proppant, K is a distance coefficient, $E_1$ and $\nu_1$ are the elastic modulus and the Poisson's ratio of proppant, respectively. $D_2$ is the thickness of the upper and lower coalbeds. | Proposed for proppant embedment in soft rock and coal. Considers the compression of the coalbed. Modified model can be found in Zhang and Hou, 2016. |
| Zhao's model (Zhao et al., 2000) | $\sigma_a = a_3 + a_4 \ln\ln h$ <br> where $a_3 = H - H(1-k)\frac{\ln\ln h_2}{\ln\ln h_2 - \ln\ln h_1}$, <br> $a_4 = \frac{H(1-k)}{\ln\ln h_2 - \ln\ln h_1}$. <br> H is the yield stress, kH is the stress at the point of initial yielding. $h_1$ and $h_2$ are the proppant indentation depths for the beginning of elastoplastic and fully-plastic deformation, respectively. | Model for the transition from elastic to plastic deformation based on contact mechanics. Suitable for elastoplastic proppant indentation. |

**Fig. 12.** Evolution of embedment trimmed for the plastic regime and the influence of friction. A quadratic template function is used for data fitting.

vertical fracture in a CBM reservoir, the overburden and horizontal tectonic stress are the same at 9 MPa. The fluid pressure is decreased from 8 MPa to 0 MPa during depletion. All important reservoir parameters are listed in Table 4.

To elucidate key feedbacks in these competitive effects, four scenarios are simulated, viz.: 1) non-sorptive gas with consideration of the variable stress-hardening effect ($h_1$); 2) sorptive gas ($CH_4$ or $CO_2$) with consideration of the variable stress-hardening effects ($h_2$); 3) non-sorptive gas without consideration of the variable stress-hardening effect ($h_3$); 4) sorptive gas without consideration of the variable stress-hardening effects ($h_4$). Fig. 15 shows the modeling results for propped fractures for these four scenarios. In Fig. 15 (A), the initial indentations are the same at 0.012 mm under an effective stress of 1.4 MPa (initial fluid pressure = 8 MPa). When the drainage begins, the changes in proppant embedment are distinctively different in these four cases. The blue curve $h_1$ (1: non-sorbing + VSH effect) shows how proppant embedment evolves as effective stress increases without the influence of gas desorption. The curve $h_3$ represents the evolution of proppant embedment without consideration of sorptive reaction and VSH effect (3: non-sorbing effect only). Comparing $h_1$ and $h_3$, it is clear that proppant indentation may be significantly overestimated if the increasing stress-hardening effect is neglected, especially when effective stress is large. At an effective stress of 9 MPa, embedment of $h_3$ is overestimated by 79% compared to $h_1$. The result indicates that during production the confinement applied to fracture walls plays an important role in diminishing the indentation generated from loading stress. Similar results can be observed in the contrast between the scenarios for $h_2$ (2: sorbing + VSH effects) and $h_4$ (4: sorbing effect only). It is also worth noting that in the comparison between $h_1$ and $h_3$, the proppant embedment of $h_1$ closely resembles the concave downwards profile in elastic zone because of the variable stress-hardening effect, though it is indeed within the elastoplastic regime.

If $CH_4$ is present within the reservoir, the embedment evolution curve first increases and then decreases at a low fluid pressure, instead of increasing monotonically. As the $CH_4$ drains, the gas-charged coal shrinks and the aperture increases, resulting in a reduction in the indented volume of proppant. This decrease in indentation demonstrates
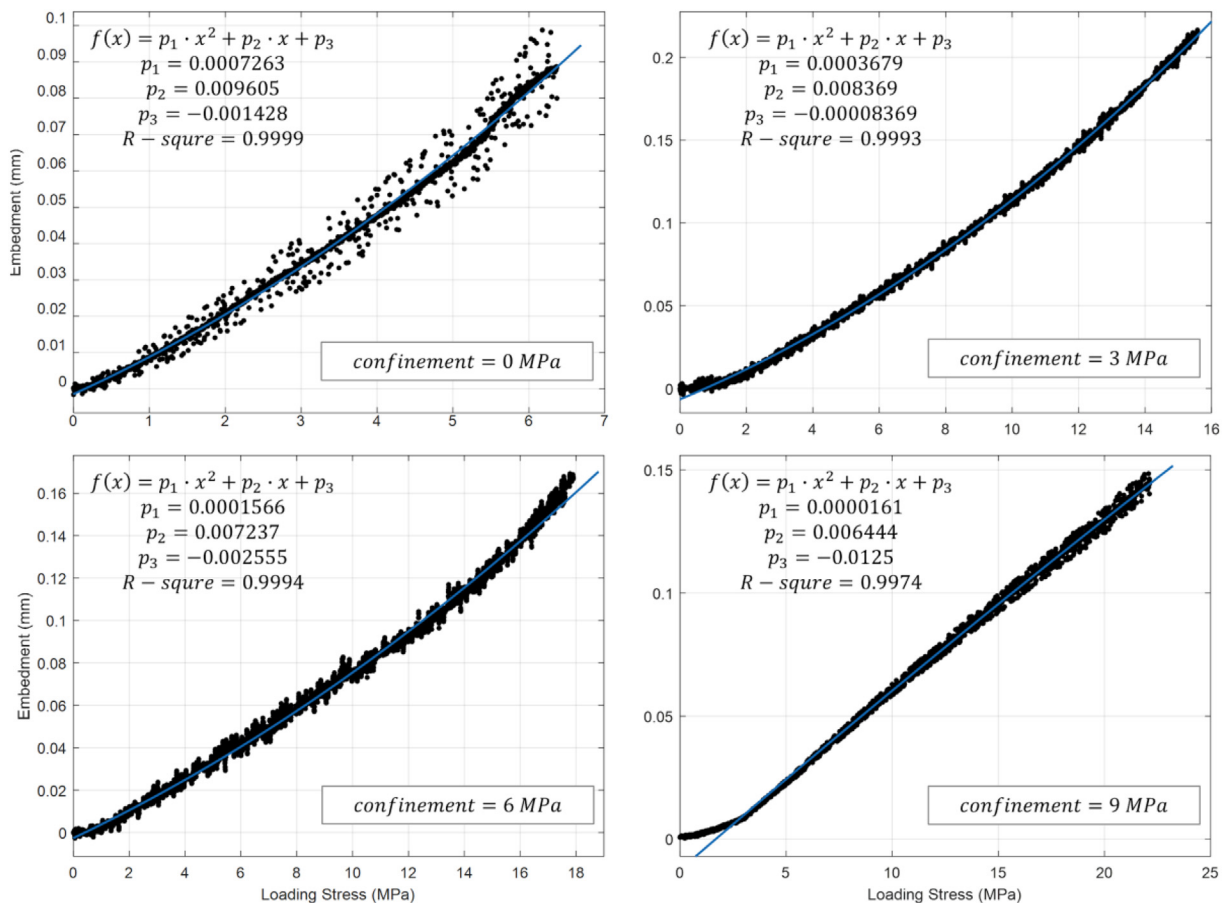


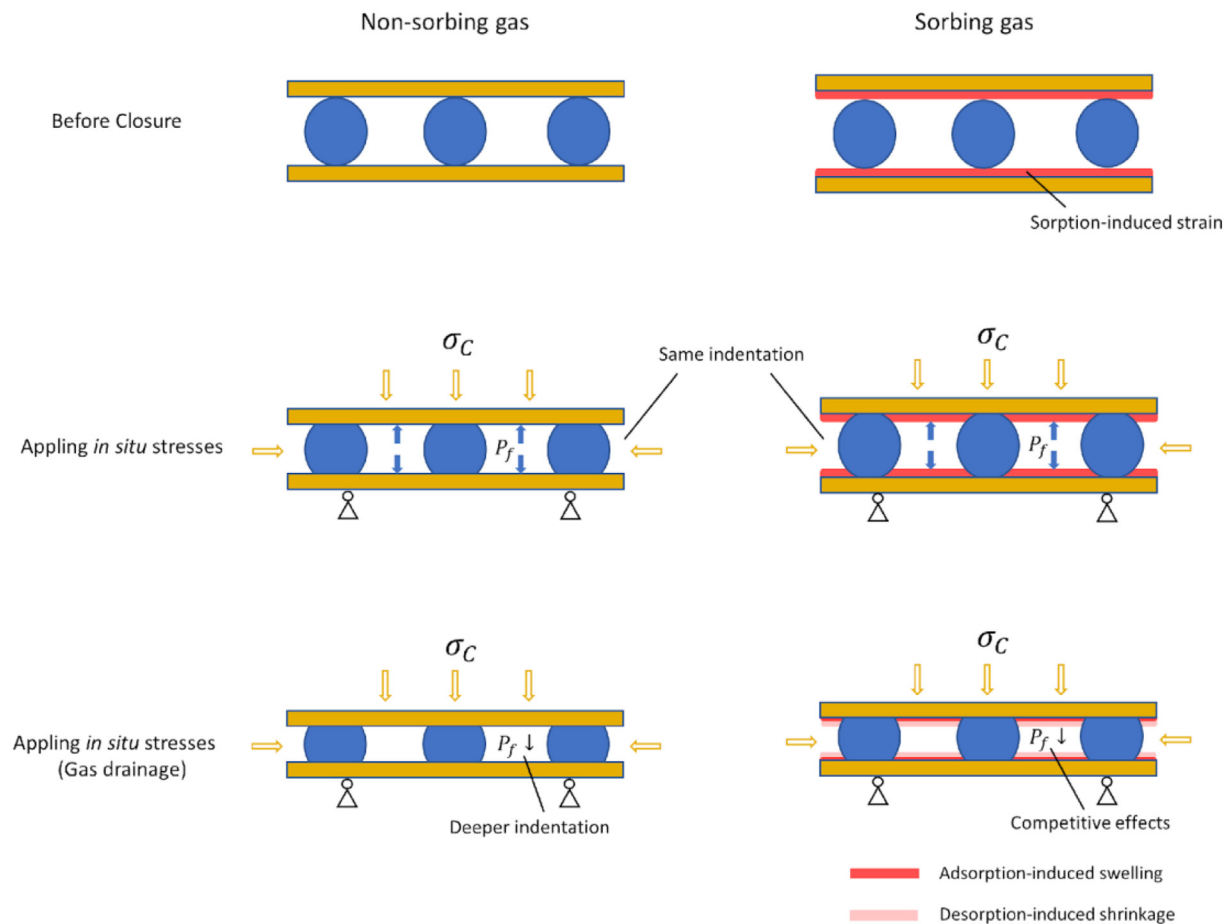**Fig. 13.** Summary of data fitting results of the experimental data.

**Fig. 14.** Schematic view during gas drainage. Effective stresses are elevated during methane recovery, increasing both normal loading stress and confinement and simultaneously overprinting sorption-induced volumetric strains. The eventual indentation is determined by these competitive effects.

**Table 4**
Modeling parameter magnitudes for coal and proppant.

| Parameter | Value |
|---|---|
| Young's modulus of coal ($E$) | 3.0 GPa |
| Biot coefficient ($\alpha$) | 0.95 |
| $CH_4$ saturation pressure ($P_f$) | 0–8 MPa |
| Initial confining stress ($\sigma_1$) | 9 MPa |
| Initial reservoir pressure ($P_{f0}$) | 8 MPa |
| Langmuir pressure constant for $CH_4$ ($P_L$) | 2.07 MPa |
| Langmuir strain constant for $CH_4$ ($\varepsilon_L$) | 0.0128 |
| Langmuir pressure constant for $CH_4$ ($P_L$) | 1.38 MPa |
| Langmuir strain constant for $CH_4$ ($\varepsilon_L$) | 0.0237 |
| Initial porosity ($\varphi_{f0}$) | 0.05 |
| Shape factor ($\beta$) | 0.32 |
| Proppant radius ($R$) | 0.32 mm |

that the effect of desorption dominates over the effect of mechanical closure. A replacement of the predominant effect in this competition can be clearly observed in the curves of h$_2$ (2: sorbing + VSH effects) and h$_4$ (4: sorbing effect only). The total revcovered indentation is 0.024 mm in h$_2$ (2: sorbing + VSH effects), which is ~12 times that in h$_4$ (4: sorbing effect only). This measurable difference results from the combination of the varying stress-hardening effect and sorption-induced shrinkage, which function together to counter proppant embedment induced by the increasing loading stress. Therefore, when the desorption effect dominates, a recovery from indentation (increment in aperture) possibly occurs during late stage methane production, causing a recovery of fracture closure.

Fig. 15 (B) shows the corresponding evolutions of propped

permeability for the four scenarios. Without considering stress-hardening effects, the reduction in permeability is largely overestimated in the propped fracture. In the comparison between scenarios 1 (1: non-sorbing + VSH effect) and 3 (3: non-sorbing effect only), for instance, a 4-fold smaller permeability is miscalculated at an effective stress of 9 MPa if stress-hardening effects are neglected. Considering the sorption effect (2: sorbing + VSH effects), the permeability begins to rebound due to the predominant effect of desorption-induced shrinkage when fluid pressure is drained to lower than 2 MPa, in this case. The other three cases present either a monotonic decrease or merely negligible recovery in the propped permeability. In the case including all the necessary considerations for real behavior (2: sorbing + VSH effects), the minimum and eventual (normalized) permeabilities are 0.24 and 0.35, respectively. The result implies that the propped fracture has the potential to facilitate methane production with a considerable permeability, even when high closure stresses are generated by fluid drainage.

In a more complex system, such as that for Microbial-ECBM and $CO_2$-ECBM reservoirs, propped fractures for the binary gas transport are influenced by the different preferential sorptions of $CO_2$ and $CH_4$ (Pan and Connell, 2007; Sampath et al., 2017; Zhi et al., 2019). It is assumed that the binary mixture sustains its proportions of each gas species and they are primarily transported through the propped fractures due to the overwhelmingly high fracture permeability compared to matrix permeability. Note that the influence of coal biodegradation on propped permeability is not discussed in this study. Given that $CH_4$ concentration is $x_i$ and $CO_2$ concentration is $(1 - x_i)$, the sorption-induced strain due to each gas species can be expressed as (Li and Elsworth, 2019; Wu et al., 2011)
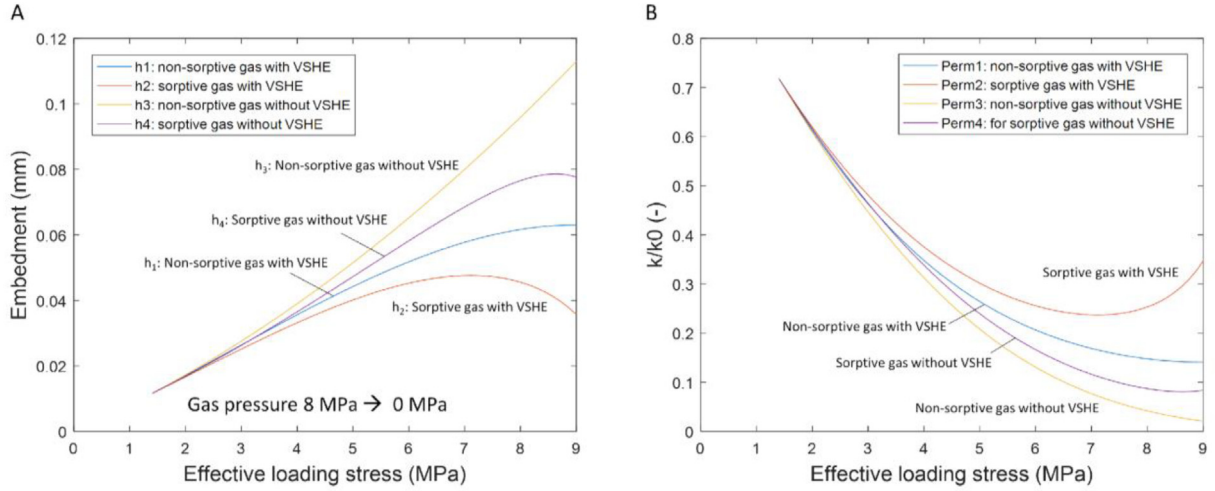
**Fig. 15.** (A) Evolution of embedment for the four scenarios of methane production; (B) Corresponding evolution of permeability.
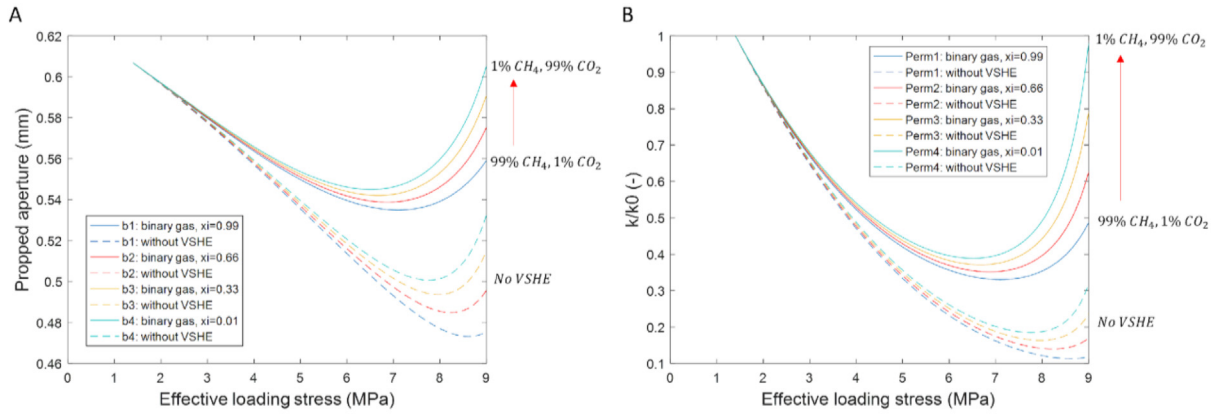


**Fig. 16.** Influence of $CH_4$ concentration versus propped aperture and permeability for a binary gas system.

$$\varepsilon_{s,i} = \varepsilon_{L,i} \frac{C_i b_i'}{1 + \sum_{i=1}^{n} C_i b_i'} \qquad (7)$$

where $C_i$ is the concentration of gas $i$, $b_i'$ is a constant coefficient to simply the extended Langmuir isotherm, $\varepsilon_{L,\ i}$ is the sorption-induced volumetric strain due to each gas species. These terms in Eq. (7) can be defined as

$$C_i = \frac{P_f}{RT} \cdot x_i \qquad (8)$$

$$b_i' = \frac{RT}{P_{L,i}} \qquad (9)$$

$$\varepsilon_{L,i} = \varepsilon_L \frac{P_f x_i}{P_{L,i} + P_f x_i} \qquad (10)$$

where $x_i$ is the partial pressure coefficient, R is the universal gas constant, T is the temperature, $P_L$ is the Langmuir pressure constant and $\varepsilon_L$ is the Langmuir strain constant.

Based on the previous assumptions, Fig. 16 shows that results for the propped aperture and the corresponding permeability in a binary gas system of $CH_4$ and $CO_2$. The solid lines show the results with consideration of the variable stress-hardening effect and the dashed lines represent the case where stress-hardening is neglected. A total of four $CH_4$ concentrations, namely 99%, 66%, 33% and 1%, are studied and the different concentrations are represented by the varying colors in Fig. 16(A). All the propped apertures decrease with an increase in the effective loading stress before the fluid pressure decreases to a

threshold pressure. In the case of 66% $CH_4$, for instance, the propped aperture ceases to decline and begins to recover when fluid pressure is drained to 2.2 MPa. The more $CO_2$ present in the binary mixture, the earlier the propped aperture begins to rebound due to its high adsorption capacity. In this study, the rebounding pressures range between 2 and 2.6 MPa, which is equivalent to effective loading stresses in the range 7.1 to 6.5 MPa, respectively. The decrease in aperture for the case of 99% $CH_4$ is up to 16% higher than that for 99% $CO_2$. Meanwhile, the higher $CO_2$ concentration results in a large recovery in aperture during drainage. If the variable stress-hardening effect is ignored, the change in propped aperture is underestimated by at most ~20%, represented by the dashed line for comparison. Fig. 16(B) shows the corresponding changes in propped permeability. Similarly, the propped permeability first decreases due to the elevated loading stress and then increases due to the predominance of sorption-induced shrinkage. For the case of 99% $CO_2$, the permeability at the conclusion of drainage almost fully recovers to its initial propped permeability, while the final permeability for 99% $CH_4$ only recovers to 48% of its initial permeability.

## 5. Conclusion

For a propped fracture, the effective loading stress normal to the fracture surface is elevated during methane production, while the effective confining stress applied laterally by the surrounding coal is also increased. Simultaneously, the change in sorption-induced strain also influences the indented volume. Experiments and numerical modeling

are conducted to illustrate the complex embedment mechanisms. Both single and multiple cycles of loading are applied to investigate the evolution of proppant embedment in coal under different scenarios – either ignoring or including the impacts of sorption and/or of stress hardening. A quadratic function is fit to the experimental data, and a semiempirical model is then derived to accommodate the effects of mechanical response and sorption-induced strain response on proppant embedment. These competitive effects are modeled and analyzed in four scenarios: (1) non-sorptive gas with consideration of the variable stress-hardening (VSH) effect; (2) sorptive gas, like $CH_4$ or $CO_2$, with consideration of VSH effect; (3) non-sorptive gas without consideration of VHS effect; (4) sorptive gas without consideration of VSH effect. Major findings are summarized as follows.

(1) Different from shale, the characteristic convex upwards profile for indentation behavior in coal is confirmed under constant confining stress. The curvature of evolution profile gradually disappears as confining stress increases. An enhancement in coal stiffness and strength are also observed due to an increasing confining stress.

(2) Confining stress plays a significant role in the cyclic loading process. After the cyclic loading test at a confining stress of 9 MPa, most indentation (~85%) is elastically recovered when the loading stress is relieved. However, maximum embedment increases with each loading cycle when unconfined, and the plastic deformation eventually destroys the integrity of the coal matrix – resulting in destruction of the sample.

(3) Proppant embedment is significantly overestimated if the variable stress-hardening effect is neglected, especially when the effective stress is large. Correspondingly, the propped permeability may be significantly underestimated (up to 4-times smaller) relative to the case where stress-hardening is incorporated as a reality.

(4) When sorptive gas is present, a reduction in indentation depth occurs during the late stages of methane production, resulting in a recovery in fracture closure (the fracture dilates). This is because the gas-charged coal reverts to its shrunk/desorbed state that causes a reduction in the indented volume of proppant and thus an opening of the fracture aperture. The resulting recovery in permeability implies that the propped coal fracture has the potential to facilitate methane production with a considerable retained permeability, even when high closure stresses are generated by fluid drainage.

(5) In a binary gas system, such as that for Microbial-ECBM and $CO_2$-ECBM reservoirs, the effectiveness of propped fractures is influenced by the relative gas concentrations of the mixture - the coal matrix shows a preference to $CO_2$ adsorption over that for $CH_4$. The greater proportion of $CO_2$ causes a smaller reduction in aperture and a larger permeability recovery during production.

## Declaration of Competing Interest

The authors declare that they have no known competing financial interests or personal relationships that could have appeared to influence the work reported in this paper.

## Acknowledgement

## References

Asef, M.R., Najibi, A.R., 2013. The effect of confining pressure on elastic wave velocities and dynamic to static Young' s modulus ratio. Geophysics 78 (3).

Bandara, K.M.A.S., Ranjith, P.G., Rathnaweera, T.D., 2019. Improved understanding of proppant embedment behavior under reservoir conditions : a review study. Powder Technol. 352, 170–192. https://doi.org/10.1016/j.powtec.2019.04.033.

Chen, D., Ye, Z., Pan, Z., Zhou, Y., Zhang, J., 2017. A permeability model for the hydraulic fracture fi lled with proppant packs under combined e ff ect of compaction and embedment. J. Pet. Sci. Eng. 149 (April 2016), 428–435. https://doi.org/10.1016/j.petrol.2016.10.045.

Geng, M., Xianbo, S., Haixiao, L., Hongyu, G., Yunqi, T., Xiao, L., 2015. Theory and technique of permeability enhancement and coal mine gas extraction by fracture network stimulation of surrounding beds and coal beds. Nat. Gas Ind. B 1 (2), 197–204. https://doi.org/10.1016/j.ngib.2014.11.012.

Guo, J., Wang, J., Liu, Y., Chen, Z., Zhu, H., 2017. Analytical analysis of fracture conductivity for sparse distribution of proppant packs. J. Geophys. Eng. 14 (3), 599–610. https://doi.org/10.1088/1742-2140/aa6215.

Hou, T., Zhang, S., Ma, X., Shao, J., He, Y., Lv, X., Han, J., 2017. Experimental and theoretical study of fracture conductivity with heterogeneous proppant placement. J. Nat. Gas Sci. Eng. 37, 449–461. https://doi.org/10.1016/j.jngse.2016.11.059.

Kogut, L., Etsion, I., 2002. Elastic-plastic contact analysis of a sphere and a rigid flat. J. Appl. Mech. 69 (September), 657–662. https://doi.org/10.1115/1.1490373.

Kumar, H., Elsworth, D., Liu, J., Pone, D., Mathews, J.P., 2015a. Permeability evolution of propped artificial fractures in coal on injection of $CO_2$. J. Pet. Sci. Eng. 133, 695–704. https://doi.org/10.1016/j.petrol.2015.07.008.

Kumar, H., Elsworth, D., Liu, J., Pone, D., Mathews, J.P., 2015b. Permeability evolution of propped artificial fractures in coal on injection of CO2. J. Pet. Sci. Eng. 133, 695–704. https://doi.org/10.1016/j.petrol.2015.07.008.

Lacy, L.L., Rickards, A.R., Bilden, D.M., 1998. Fracture width and embedment testing in soft reservoir sandstone. SPE Drill. Completion 13 (1), 25–29. https://doi.org/10.2118/36421-PA.

Lee, D.S., Elsworth, D., Yasuhara, H., Weaver, J.D., Rickman, R., 2010. Experiment and modeling to evaluate the effects of proppant-pack diagenesis on fracture treatments. J. Pet. Sci. Eng. 74 (1–2), 67–76. https://doi.org/10.1016/j.petrol.2010.08.007.

Li, Z., Elsworth, D., 2019. Controls of $CO_2$–$N_2$ gas fl ood ratios on enhanced shale gas recovery and ultimate $CO_2$ sequestration. J. Pet. Sci. Eng. 179 (December 2018), 1037–1045. https://doi.org/10.1016/j.petrol.2019.04.098.

Li, L., Gu, J., 2009. An analytical solution for the unloading in spherical indentation of elastic – plastic solids. Int. J. Eng. Sci. 47 (3), 452–462. https://doi.org/10.1016/j.ijengsci.2008.10.002.

Li, K., Gao, Y., Lyu, Y., Wang, M., 2015. New mathematical models for calculating proppant embedment and fracture conductivity. SPE J. 20 (3), 496–507. https://doi.org/10.2118/155954-PA.

Li, Y., Meng, W., Rui, R., Wang, J., Jia, D., Chen, G., ... Dandekar, A., 2018. The calculation of coal rock fracture conductivity with Different Arrangements of proppants. Geofluids 2018.

Wu, Yu, Liu, J., Chen, Z., Elsworth, D., Pone, D., 2011. A dual poroelastic model for $CO_2$-enhanced coalbed methane recovery. Int. J. Coal Geol. 86, 177–189. https://doi.org/10.1016/j.coal.2011.01.004.

Morcote, A., Mavko, G., Prasad, M., 2010. Dynamic elastic properties of coal. Geophysics 75 (6).

Mueller, M., Amro, M., Freiberg, T.U.B., 2015. Indentaion Hardness for Improved Proppant Embedment Prediction in Shale.

Pan, Z., Connell, L.D., 2007. A theoretical model for gas adsorption-induced coal swelling. Int. J. Coal Geol. 69 (4), 243–252. https://doi.org/10.1016/j.coal.2006.04.006.

Penny, G.S., 1987. An evaluation of the effects of environmental conditions and fracturing fluids upon the long-term conductivity of proppants. SPE J. 229–244.

Penny, G., Zelenev, A., Champagne, L., Chemical, C., Crafton, J., Sciences, P., 2012. Proppant and fluid selection to optimize performance of horizontal shale fracs. SPE J. 341–350. https://doi.org/10.2118/152119-MS.

Sampath, K.H.S.M., Perera, M.S.A., Ranjith, P.G., Matthai, S.K., Rathnaweera, T., Zhang, G., Tao, X., 2017. CH 4 CO 2 gas exchange and supercritical CO 2 based hydraulic fracturing as CBM production-accelerating techniques: a review. J. CO2 Util. 22 (August), 212–230. https://doi.org/10.1016/j.jcou.2017.10.004.

Song, Z., Komvopoulos, K., 2013. Mechanics of materials elastic – plastic spherical indentation: deformation regimes, evolution of plasticity, and hardening effect. Mech. Mater. 61, 91–100. https://doi.org/10.1016/j.mechmat.2013.01.003.

Stoddard, T., Mclennan, J., Moore, J., 2011. Fracture Conductivity of a Bauxite-Propped Geothermal System at In-Situ Conditions.

Tang, Y., Ranjith, P.G., 2018. An experimental and analytical study of the effects of shear displacement, fluid type, joint roughness, shear strength, friction angle and dilation angle on proppant embedment development in tight gas sandstone reservoirs. Int. J. Rock Mech. Min. Sci. 107 (May), 94–109. https://doi.org/10.1016/j.ijrmms.2018.03.008.

Volk, L., Raible, C., Carroll, H., Spears, J., 1981. Embedment of high strength proppant into low-permeability reservoir rock. Proc. SPE. https://doi.org/10.2118/9867-MS.

Wang, S., Elsworth, D., Liu, J., 2011. Permeability evolution in fractured coal : the roles of fracture geometry and water-content. Int. J. Coal Geol. 87 (1), 13–25. https://doi.org/10.1016/j.coal.2011.04.009.

Wang, S., Elsworth, D., Liu, J., 2013. Mechanical behavior of methane infiltrated coal: the roles of gas desorption, stress level and loading rate. Rock Mech. Rock Eng. 945–958. https://doi.org/10.1007/s00603-012-0324-0.

Wanniarachchi, W.A.M., Ranjith, P.G., Perera, M.S.A., 2017. Shale gas fracturing using foam-based fracturing fluid: a review. Environ. Earth Sci. 76 (2), 1–15. https://doi.org/10.1007/s12665-017-6399-x.

Wu, Yanting, Pan, Z., Zhang, D., Down, D.I., Lu, Z., Connell, L.D., 2018. Experimental study of permeability behaviour for proppant supported coal fracture. J. Nat. Gas Sci. Eng. 51 (November 2017), 18–26. https://doi.org/10.1016/j.jngse.2017.12.023.

Zhang, J., Hou, J., 2016. Theoretical conductivity analysis of surface modification agent treated proppant II – Channel fracturing application. Fuel 165, 28–32. https://doi.org/10.1016/j.fuel.2015.10.026.

Zhao, Y., Maietta, D.M., Chang, L., 2000. An asperity microcontact model incorporating the transition from elastic deformation to fully plastic flow. J. Tribol. 122 (January).

Zhi, S., Elsworth, D., Wang, J., Gan, Q., Liu, S., 2018. Hydraulic fracturing for improved nutrient delivery in microbially-enhanced coalbed-methane (MECBM) production. J. Nat. Gas Sci. Eng. 60 (August), 294–311. https://doi.org/10.1016/j.jngse.2018.10.012.

Zhi, S., Elsworth, D., Liu, L., 2019. W-shaped permeability evolution of coal with supercritical CO 2 phase transition. Int. J. Coal Geol. 211 (May), 103221. https://doi.org/10.1016/j.coal.2019.103221.